Materials & Design 270 (2026) 116856

Contents lists available at ScienceDirect

Materials & Design

journal homepage: www.elsevier.com/locate/matdes

Loading-mode-dependent deformation mechanisms of sintered porous Cu

Chenshan Gao [a], Leiming Du [b], Tianxing Du [b], Qihang Zong [a], Shizhen Li [a], Huiru Yang [c], Guoqi Zhang [a], Huaiyu Ye [a,b,d,*]

[a] School of Microelectronics, Southern University of Science and Technology, 1088 Xueyuan Avenue, Shenzhen, 518055, China
[b] Department of Microelectronics, Delft University of Technology, Mekelweg 4, Delft, 2628 CD, Netherlands
[c] School of Electronic and Communication Engineering, Shenzhen Polytechnic University, 7098 Liuxian Avenue, Shenzhen, 518055, China
[d] State Key Laboratory of Quantum Functional Materials, School of Microelectronics, Southern University of Science and Technology, 1088 Xueyuan Avenue, Shenzhen, 518055, China

HIGHLIGHTS

- Particle size decouples elastic stiffness from yield strength in sintered porous Cu.
- Large-particle structures show higher apparent modulus due to improved load-path continuity.
- Small-particle structures exhibit higher yield strength through distributed neck deformation and pore compaction.
- Coarse necks and continuous remaining ligaments enhance fracture resistance under bending.
- MD simulations reveal that closely spaced necks promote dislocation arrest, stacking-fault accumulation, and distributed plasticity.

ARTICLE INFO

Keywords:
Porous Cu
Micromechanics
Size effect
Fracture toughness
Molecular dynamics

ABSTRACT

Sintered porous Cu contains a heterogeneous particle-neck-pore architecture whose deformation depends strongly on loading mode. In this study, porous Cu structures prepared from small particles (184 nm) and large particles (1451 nm) were examined using micropillar compression, micro-cantilever bending, scanning electron microscopy (SEM), transmission electron microscopy (TEM), and molecular dynamics (MD) simulations. Under compression, the large-particle structure exhibited a higher apparent elastic modulus (14.5 ± 0.9 GPa) than the small-particle structure (12.7 ± 0.5 GPa), whereas the small-particle structure showed an approximately 80% higher yield strength (364 ± 58 versus 202 ± 71 MPa). In contrast, the large-particle structure exhibited an approximately 245% higher conditional fracture toughness (5.56 ± 0.14 versus 1.61 ± 0.16 $MPa \cdot m^{1/2}$) and 1270% higher total bending work (8823 ± 1245 versus 644 ± 164 pJ). Microstructural analyses revealed that the refined particle-neck network accommodated compression through distributed pore compaction, neck deformation, and dislocation accumulation, suppressing strain localization. The coarser network promoted intraparticle slip and interfacial sliding under compression, while enhancing remaining-ligament continuity and neck bridging during crack propagation. MD simulations reproduced these distinct compressive responses and defect-evolution characteristics. These findings provide guidance for optimizing particle-neck-pore architectures in reliable sintered Cu interconnects.

1. Introduction

Sintered Cu with porous structure has emerged as a promising material for advanced microelectronic [1,2] and power-electronic packaging applications [3–6], owing to its high thermal conductivity [7–11], high-temperature stability [12,13], and cost advantage [7,12]. Compared with conventional solder-based interconnects [14–17], sintered Cu can form a high-melting-point metallic porous structure through relatively low-temperature processing. Considerable efforts have therefore been devoted to Cu particle design, sintering conditions, oxidation control, densification behavior, and thermal, electrical, and mechanical performance [6,18]. However, the mechanical behavior of sintered Cu porous structures remains insufficiently understood, particularly how the initial particle size modifies the load-bearing neck-pore network and thereby affects stiffness, yielding, and fracture resistance at the microscale.

* Corresponding author at: School of Microelectronics, Southern University of Science and Technology, 1088 Xueyuan Avenue, Shenzhen, 518055, China.
Email address: yehy@sustech.edu.cn (H. Ye).

https://doi.org/10.1016/j.matdes.2026.116856
Received 26 June 2026; Received in revised form 2 August 2026; Accepted 19 August 2026
Available online 20 August 2026
0264-1275/

The motivation for examining particle-size effects stems from the particle-derived architecture of low-temperature sintered Cu. During sintering, incomplete coalescence produces a porous load-bearing network consisting of sintered necks [19,20], grain boundaries [21], and residual pores [22,23]. As a result, the mechanical response of sintered Cu differs markedly from that of fully dense Cu [24,25]. In bulk Cu, strength and deformation are commonly discussed in relation to grain size [26,27], twin-boundary spacing [28–30], and structural gradients [29,31–33], because these microstructural length scales regulate dislocation nucleation, storage, and transmission [28–30,34]. At smaller dimensions, micro- and submicron-sized metallic specimens may further exhibit external size effects, where limited specimen volume constrains dislocation multiplication and storage, giving rise to source-limited plasticity or dislocation starvation [35–38]. For sintered Cu, the relevant length scale is different. The starting particle size is not simply a crystallographic length scale, nor is it equivalent to the external dimension of a micro-specimen. Rather, it is a processing-defined structural parameter that determines the initial packing configuration and subsequently influences neck formation, pore spacing, interparticle contact density, and the continuity of load-bearing ligaments [39–41]. These coupled structural features are expected to control local stiffness [42], yielding [22], and fracture resistance [20,43] through their effects on neck connectivity, pore distribution, and the integrity of the remaining solid framework [6]. Particle size in sintered Cu therefore represents a distinct form of size effect, separate from those commonly considered in additively manufactured structures and small-scale crystals [44,45]. Importantly, changing particle size does not vary a single structural variable in isolation; it simultaneously modifies several features of the neck-pore network. It remains unclear whether stiffness, yielding, and fracture resistance are governed by the same particle-derived architecture, or whether each response is controlled by different structural features within the sintered Cu network.

Previous studies on Cu particle size have primarily focused on processing and joint-level performance, including sinterability, packing density, densification, and shear strength in sintered Cu structures [46–49]. This emphasis is well justified, because smaller Cu particles generally facilitate low-temperature neck formation through their higher surface area and shorter diffusion length [50–53]. Meanwhile, micro/nano mixed or bimodal Cu particle systems can improve packing efficiency and promote more continuous neck-connected pathways, thereby enhancing Cu–Cu joint strength and overall interconnect performance [3,6]. In this context, Yonezawa et al. [47] identified particle-size engineering as a central strategy, highlighting its influence on both sintering kinetics and the final porous structure. Atomistic simulations have further confirmed that Cu nanoparticle size affects coalescence behavior, neck growth, and microstructural evolution during Cu–Cu bonding [50,54]. Moreover, micromechanical studies have shown that pore morphology, ligament continuity, and specimen size can strongly influence the measured response of porous sintered materials [55,56]. For example, Chen et al. [56] demonstrated that the fracture toughness obtained from microporous sintered Ag micro-cantilevers depends on the ratio between specimen dimensions and the pore-network length scale. In sintered Cu nanoparticles, pressure-assisted sintering can generate anisotropic neck alignment, non-uniform areal density, and direction-dependent mechanical strength [57], while interface-notched micro-cantilever studies indicate that interparticle bonding and crack-path selection play critical roles in fracture behavior [43]. These findings suggest that particle size should not be considered only as a processing parameter for improving sintering or joint strength [49]. Rather, it may alter the structural units that control different micromechanical responses. To further link the experimentally observed mechanical responses to their atomistic origins, molecular dynamics (MD) were employed to resolve atomic diffusion, interparticle neck formation, defect nucleation, stacking-fault evolution, and local pore collapse during sintering and subsequent deformation [57]. However, their limited spatial and temporal scales, together with the correspondingly high loading rates, prevent direct quantitative prediction of macroscopic mechanical properties and long-term service behavior. MD is therefore used primarily to identify comparative particle-size- and morphology-dependent deformation trends and elucidate their underlying atomistic mechanisms. Accordingly, it has been widely adopted as a complementary tool in Cu-sintering research for interpreting microstructural evolution and deformation behavior [19,57,58].

In this study, sintered Cu was prepared from two monomodal spherical particle systems: nano-Cu particles (184 nm) and micro-Cu particles (1451 nm). Micropillar compression and micro-cantilever bending tests were employed to examine the particle-size-dependent responses under compression- and fracture-dominated local stress states. Scanning electron microscopy (SEM), transmission electron microscopy (TEM), and molecular dynamics (MD) simulations were used to correlate the measured mechanical behavior with neck-pore morphology, particle bonding, local crystallography, and deformation localization. By combining these complementary experimental and simulation approaches, this work clarifies how particle size influences apparent stiffness, compressive yielding, and fracture resistance in sintered porous Cu, and provides a micromechanical basis for particle-size selection under different reliability-relevant loading conditions.

2. Experimental and simulation methods

2.1. Sintered sample preparation

Fig. 1 shows the sintering process and initial particle characteristics of the pressure-assisted sintered Cu samples. Cu pastes containing either nano- or micro-Cu particles were first transferred into a sintering mold (Fig. 1a). The filled mold was then heated to remove the organic solvent from the paste (Fig. 1b), followed by pressure-assisted sintering

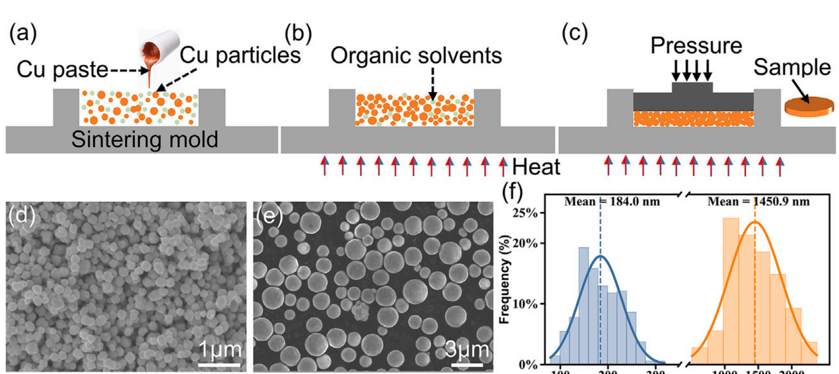

Fig. 1. Sintering process and initial particle characteristics of Cu particles: (a) filling of Cu paste into the sintering mold; (b) solvent removal by heating; (c) pressure-assisted sintering under uniaxial loading; SEM images of the initial (d) nano-Cu and (e) micro-Cu particles, and (f) corresponding particle-size distributions.

under uniaxial loading to obtain the consolidated Cu sample (Fig. 1c). The local areal pore fractions of the resulting sintered structures were quantified from cross-sectional TEM images using ImageJ and were measured to be 5.28% and 3.16% (shown in Fig. S1) for the small- and large-particle samples, respectively. The starting powders consisted of two monomodal spherical Cu particle systems, namely nano-Cu particles (Fig. 1d) and micro-Cu particles (Fig. 1e). The corresponding particle-size distributions confirm the clear separation between the two systems, with diameters of 184 ± 45 nm and 1451 ± 395 nm, respectively (Fig. 1f). The two particle systems were selected to establish a clear comparison between submicrometer and micrometer Cu powders. Monomodal powders were used to avoid the additional packing, densification, and sintering effects introduced by bimodal particle mixtures. Accordingly, the present study compared two discrete particle-size regimes to identify their respective deformation mechanisms, rather than to establish a continuous particle-size dependence.

2.2. Micromechanical tests

Micropillars and notched micro-cantilevers were fabricated from the sintered Cu samples by focused ion beam (FIB) milling using a dual-beam FEI Helios G4 CX FIB-SEM system for micropillar compression tests and micro-cantilever bending tests, respectively [59–61]. All specimens were extracted from the interior regions of the sintered samples to minimize edge-related effects associated with pressure-assisted sintering. Cylindrical micropillars were prepared by annular milling [62–64], followed by successive low-current polishing steps to reduce side-wall tapering, redeposition, and ion-beam-induced damage. Notched micro-cantilevers were fabricated by trench milling to define the beam geometry, followed by oblique underside milling from both sides to release the beam and low-current polishing to improve geometrical symmetry [65–67]. A notch was then introduced near the fixed end by line milling. The final specimen geometries were characterized by SEM before testing, and the measured dimensions were used for all subsequent stress, strain, and fracture-resistance calculations.

Micropillar compression tests and micro-cantilever bending tests were performed at room temperature using an in situ nanoindenter system (Alemnis AG, Switzerland) mounted inside a Zeiss Ultra 55 FEG-SEM. The micromechanical testing configuration and representative specimen geometries are shown in Fig. 2. For micropillar compression, cylindrical micropillars with a nominal diameter D of 5 μm and height H of 12.5 μm were used, corresponding to an aspect ratio H/D of 2.5, as shown in Fig. 2(b) and Table S1. Uniaxial compression was performed under displacement control using a flat-punch diamond tip with a nominal radius of 10 μm at a constant displacement rate of 10 nm s^{-1}. Before loading, the specimens were carefully leveled and aligned under SEM observation to ensure axial loading and minimize bending or eccentric effects. A small pre-load was applied to establish stable contact between the punch and the pillar surface and to reduce the influence of surface irregularities. The load–displacement data were continuously recorded

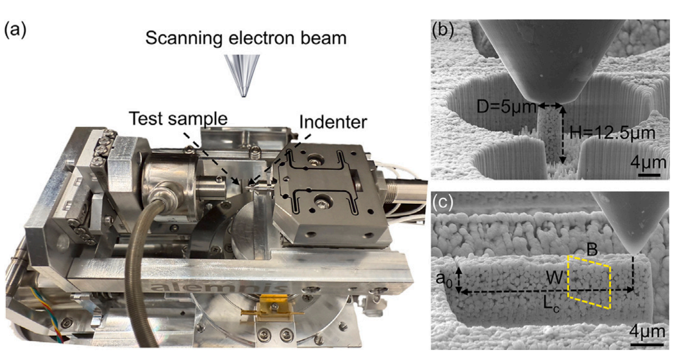

Fig. 2. (a) micromechanical test setup; SEM images of the (b) micropillar and (c) micro-cantilever.

during compression, followed by active unloading at the end of the test. The engineering compressive stress and strain were calculated from the measured load-displacement data based on the initial pillar geometry. These quantities were used to compare the compressive responses of the two sintered Cu systems, rather than to represent homogeneous stress and strain states during large deformation.

For micro-cantilever bending tests, the key geometrical parameters (as shown in Table S2) include notch length (a_0), bending moment arm (L_c), beam width (B), and beam depth (W) as indicated in Fig. 2(c). Here, L_c denotes the distance from the notch plane to the loading point, W is the width along the notch front, B is the beam depth in the bending direction and a_0 is the notch length measured from the fracture surface. Before testing, the indenter tip was positioned at the loading point defined by L_c under SEM observation. Bending was performed under displacement control using a conospherical diamond tip with a radius of 1 μm at a constant displacement rate of 10 nm s^{-1}. The load–displacement data were continuously recorded through the peak-load and post-peak stages until fracture or the end of the prescribed test. The conditional fracture toughness, expressed as K_Q, was estimated from the maximum load and beam geometry as follows [56]:

$$K_Q = \frac{P_{\max} L_c}{B W^{3/2}} f\left(\frac{a_0}{W}\right) \tag{1}$$

where $P_{\max}$ is the maximum load, and $f(a_0/W)$ is the geometry correction factor [68,69]. Because the micrometre-scale cantilever dimensions did not satisfy the dimensional and crack-tip constraint requirements for a valid plane-strain fracture toughness K_{IC}, the calculated values are reported as conditional K_Q and used to compare the two structures tested under the same micro-cantilever configuration [70,71]. This limitation is particularly relevant for sintered Cu, where the cantilever dimensions, notch geometry, crack-tip plastic zone, and microstructural length scales can be comparable. Residual pores, sintered necks, and particle units may also be of similar scale to the crack-tip process zone and the remaining load-bearing ligament. Therefore, K_Q is used here as a comparative measure of fracture resistance under the same micro-cantilever geometry.

2.3. Microstructure characterization

SEM, TEM, precession electron diffraction (PED), and transmission Kikuchi diffraction (TKD) were used to characterize the morphology, microstructure, and deformation features of the sintered Cu specimens (analyzed by OIM Analysis software). SEM was employed to examine the morphologies of the micropillars and micro-cantilevers before and after micromechanical tests, providing direct evidence of specimen geometry, deformation mode, and fracture morphology. TEM observations were performed on deformed regions to resolve local microstructural changes and deformation features at the nanoscale. PED was used to characterize the crystallographic structure of sintered necks in the small-particle sintered Cu, thereby providing orientation information associated with neck formation and particle bonding. The crystallographic grain-size distribution of the as-sintered small-particle structure was quantified from the PED orientation map using MapViewer software. Grain boundaries were identified using a misorientation threshold of 5°, and a minimum grain size of 30 nm was applied. The area-based grain-size statistics were obtained from 733 identified grains within the analyzed PED region. TKD was conducted on TEM lamellae prepared from deformed micropillars to analyze particle-scale deformation morphology, local crystallographic orientation, grain-boundary distribution, and orientation gradients after compression.

2.4. MD simulation

MD simulations were performed to support the mechanistic interpretation of particle-scale deformation. The particle construction and sintering configuration were adopted from our previous protocol [57]. The initial particle assemblies were generated by randomly selecting the particle centers within the three-dimensional simulation cell, while the particle radii were sampled from normal distributions corresponding to the prescribed particle-size ranges. For each newly generated particle, overlap with both the existing particles and their periodic images was examined to ensure geometrical consistency across the simulation-cell boundaries. Each particle was subsequently assigned a random crystallographic orientation. This procedure was repeated until the acceptance rate for inserting additional particles became negligible. Selected particles were then isotropically expanded until contact with neighboring particles was established, followed by energy minimization using the conjugate-gradient algorithm to eliminate residual atomic overlap and high-energy local configurations. To reproduce the relative density of the large-particle experimental specimens, the large-particle models were assigned a larger z-dimension than the corresponding small-particle models. The Cu particle diameters were 40 ± 20 Å and 90 ± 10 Å for the small- and large-particle models, respectively; the corresponding model dimensions were 300 Å × 300 Å × 1500 Å and 300 Å × 300 Å × 2000 Å. The initial unsintered configurations and corresponding longitudinal cross-sectional views of the small- and large-particle MD models are presented in Fig. S2, confirming the distinct particle-size regimes prescribed during model construction. All generated models contained more than 3.5 million atoms, providing a sufficiently large simulation domain to reduce finite-size effects and capture representative deformation behavior. Following sintering, the particle assemblies were sectioned into cylindrical pillar models with aspect ratios matching the experimental specimens. All models were energy-minimized and equilibrated at 300 K in an NVT ensemble for 20 ps before mechanical loading. Compression was applied along the z-direction at an engineering strain rate of 1×10^9 s^{-1} to a total strain of 30%. The deformed systems were subsequently relaxed at 300 K for 50 ps to facilitate stress redistribution and structural equilibration.

3. Results and discussion

3.1. Micropillar compression test

Micropillar compression tests were performed to assess the compressive mechanical response of the sintered Cu structures. As shown in Fig. 3(a) and (b), both samples exhibit a well-defined initial linear regime, followed by a yield transition and subsequent nonlinear plastic deformation. The apparent elastic modulus was determined from the slope of the initial linear portion of each engineering stress-strain curve, while the yield strength was extracted using the conventional 0.2% offset method [72,73]. The stress drops observed at the end of the curves correspond to active unloading during testing and therefore should not be interpreted as structural instability or fracture. Compared with the large-particle sample, the small-particle sample sustains higher stresses over most of the plastic deformation range, with several curves reaching approximately 700–850 MPa at strains above 30%. In contrast, the large-particle sample generally exhibits lower flow stresses, mostly below about 600 MPa before unloading, indicating easier post-yield deformation. The statistical results in Fig. 3(c) and (d) further show that the apparent elastic modulus and yield strength follow opposite trends. The elastic modulus increases from 12.7 ± 0.5 GPa for the small-particle sample to 14.5 ± 0.9 GPa for the large-particle sample, suggesting a higher initial resistance to small-strain elastic deformation in the coarser sintered network. However, the yield strength decreases markedly from 364 ± 58 MPa for the small-particle sample to 202 ± 71 MPa for the large-particle sample. Notably, the yield strength of the small-particle monomodal structure also exceeds the approximately 120–320 MPa range reported by Du et al. for bimodal sintered Cu [19]. This comparison shows that a high compressive yield response can be achieved in the fine monomodal system without introducing the additional particle-ratio, packing, and contact-topology variables inherent to bimodal mixtures. This contrast indicates that the refined particle-neck network enhances resistance to the plastic deformation, consistent with size-dependent strengthening commonly observed in micro- and nanoscale metallic structures [74,75]. Nevertheless, the simultaneous decrease in apparent elastic modulus and increase in yield strength in the small-particle sample indicate that the initial elastic stiffness and the resistance to plastic yielding are governed by distinct microstructural factors; the underlying deformation mechanism will be further elucidated through subsequent SEM observations.

Fig. 4 presents the post-compression morphologies and corresponding deformation models. For the small-particle structure, the compressed micropillar largely retains its cylindrical geometry, while a moderate waist-like deformation zone is formed near the middle region of the pillar (Fig. 4a and b). The initially porous particle network becomes visibly compacted after compression, indicating that deformation is mainly accommodated by pore closure, local particle rearrangement and plastic deformation of the interconnected necks. No obvious large-scale separation or dominant side cracking is observed in the examined region. As schematically illustrated in Fig. 4(c), the small-particle network contains

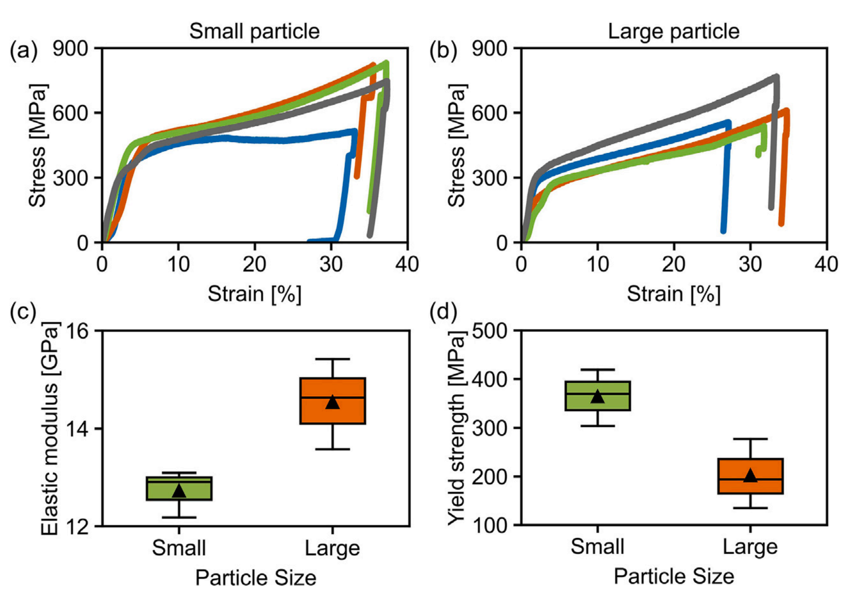

Fig. 3. Micropillar compression response of sintered Cu structures with different particle sizes: engineering stress–strain curves for (a) small-particle and (b) large-particle samples, and the corresponding (c) elastic modulus and (d) yield strength.

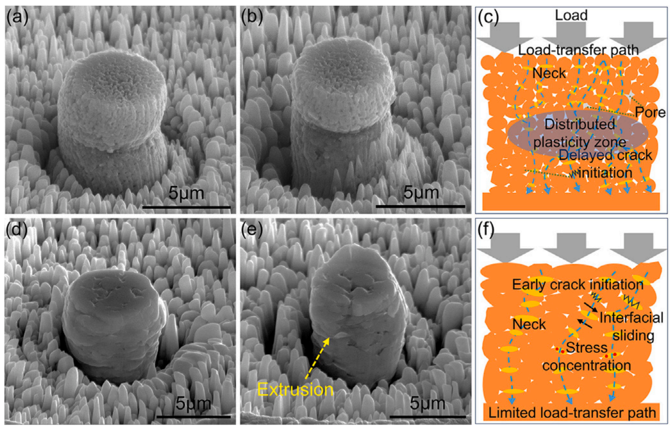

Fig. 4. Post-compression deformation characteristics of sintered Cu micropillars with different particle sizes: (a, b) SEM morphologies of the small-particle structures; (d, e) SEM morphologies of the large-particle structures, with corresponding schematic deformation mechanisms shown in (c) and (f), respectively.

abundant pores with sizes comparable to the constituent particles, together with a relatively dense population of interparticle necks. Such a structural configuration provides multiple load-transfer paths and allows local shear deformation to be distributed over a broader volume. The uniformly distributed pores can also serve as accommodation space for network compaction, which reduces the tendency for deformation to concentrate at a single neck or interface.

In contrast, the large-particle micropillar exhibits more pronounced particle-scale deformation after compression (Fig. 4d and e). The pillar is compacted, but local particle extrusion, separation features and visible side cracking can be identified, indicating that the post-yield deformation is more spatially localized. The schematic model in Fig. 4(f) suggests that the coarser network contains fewer effective load-transfer paths, so the applied load is more readily concentrated at large necks, particle-derived interfaces and pore edges. Once yielding begins, interfacial sliding and local displacement can develop over larger structural units, promoting stress concentration and crack initiation. This morphology explains why the large-particle structure shows a higher apparent elastic modulus but a lower yield strength: the coarse skeleton provides stronger initial resistance to elastic deformation, whereas its limited structural redundancy facilitates localized plastic flow after yielding. Similar size-dependent plasticity and localized deformation have been widely reported in microscale metallic systems, where reduced structural dimensions and constrained dislocation activity can strongly modify the apparent strength and deformation mode [76]. Therefore, Fig. 4 provides morphological evidence that the opposite trends in elastic modulus and yield strength arise from different deformation mechanisms before and after yielding, while the detailed crack initiation and interfacial sliding processes require further confirmation from higher-resolution SEM observations.

3.2. Micro-cantilever bending test

Micro-cantilever bending tests were further conducted to evaluate the fracture resistance of the two sintered Cu structures. As shown in Fig. 5(a) and (b), the small- and large-particle samples exhibit markedly different load-displacement responses. For the small-particle sample, the load increases rapidly during the initial bending stage and reaches a maximum load of 500 ± 29 μN at a peak displacement of 0.92 ± 0.10 μm (Fig. 5a and c), followed by a relatively steep post-peak load decrease. This response indicates that once the crack initiates from the notch, the remaining ligament can only sustain limited stable crack growth. In contrast, the large-particle sample reaches a much higher maximum load of 1700 ± 90 μN, approximately 3.4 times that of the small-particle sample, and the peak occurs at a larger displacement of 2.07 ± 0.21 μm (Fig. 5b and c). More importantly, the large-particle curves retain a considerable load over an extended displacement range after the peak, suggesting more stable crack propagation and higher resistance to bending-induced damage accumulation. The conditional fracture toughness, K_Q, is summarized in Fig. 5(d). The small-particle sample exhibits a K_Q of $1.61 \pm 0.16\ \mathrm{MPa \cdot m^{1/2}}$, whereas the large-particle sample reaches $5.56 \pm 0.14\ \mathrm{MPa \cdot m^{1/2}}$. This pronounced increase indicates that fracture under the notched micro-cantilever configuration is controlled by ligament continuity ahead of the notch and crack-propagation stability within the particle-derived network, rather than by compressive yield strength alone. This explains why the large-particle structure, despite its lower compressive yield strength (Fig. 3), shows higher resistance to bending-induced fracture (Fig. 5).

In addition, the area under the load–displacement curve was used to quantify the external work consumed during micro-cantilever fracture. The total bending work (W_b) was calculated as [69]:

$$W_b = \int_0^{\delta_f} P(\delta)\, \mathrm{d}\delta \tag{2}$$

where W_b is the total external work during bending fracture, $P(\delta)$ is the load as a function of displacement curve, and δ_f is the displacement at fracture or at the end of the test.

The energy absorption behavior is consistent with the higher fracture resistance of the large-particle structure. The total bending work, obtained from the area under the load-displacement curve, increases from 644 ± 164 pJ for the small-particle sample to 8823 ± 1245 pJ for the large-particle sample. This increase is dominated by the post-peak contribution, which rises from 378 ± 123 pJ to 6322 ± 1461 pJ, accompanied by an increase in the post-peak work fraction from 58% to 71%. These results indicate that the large-particle structure not only sustains a higher peak load but also retains load-bearing capacity more effectively during crack propagation. Therefore, its higher conditional toughness is mainly associated with stable post-peak deformation and greater energy dissipation within the remaining ligament.

The post-bending fracture morphologies in Fig. 6 further clarify the origin of the different load-retention behaviors during notched micro-cantilever bending. In the small-particle sample, the fracture region consists of fine particle-neck units and densely distributed residual pores (Fig. 6a and b). Such a highly segmented network reduces the continuity of the remaining ligament ahead of the notch, allowing local damage to connect neighboring pores and fine necks over short distances. This promotes rapid ligament degradation after crack initiation and is consistent with the steep post-peak load drop observed in Fig. 5(a). By contrast, the large-particle sample exhibits coarser particle-derived units and more pronounced local deformation near the fracture region (Fig. 6c and d). The crack path appears to be deflected or interrupted by larger necks and particle interfaces, indicating that crack advance requires progressive separation of relatively coarse load-bearing units. These features can provide local bridging and maintain partial load transfer across the remaining ligament during crack propagation. This fracture mode differs from that of dense bulk metals, where crack resistance is commonly governed by crack-tip plasticity, void growth and coalescence; in the present sintered Cu structures, the fracture response is additionally controlled by the connectivity and characteristic length scale of the particle-neck-pore network. Similar ligament-size and connectivity effects have been reported in porous metallic networks [71,77].

3.3. TEM analysis

Fig. 7 shows the TEM morphologies of the small- and large-particle sintered Cu structures after micropillar compression, providing direct evidence for particle-scale deformation and local strain accommodation. In both samples, the particle-derived networks are visibly compacted after loading, and the initially irregular particles become flattened along the

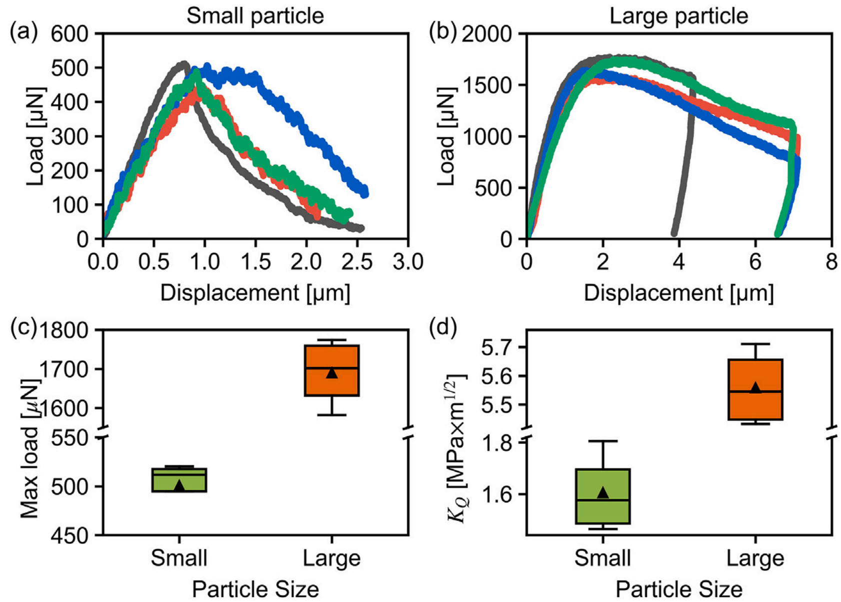

Fig. 5. Micro-cantilever bending behavior of sintered Cu structures with different particle sizes: load-displacement curves of the (a) small-particle and (b) large-particle samples, and corresponding statistics of (c) maximum load and (d) conditional fracture toughness.

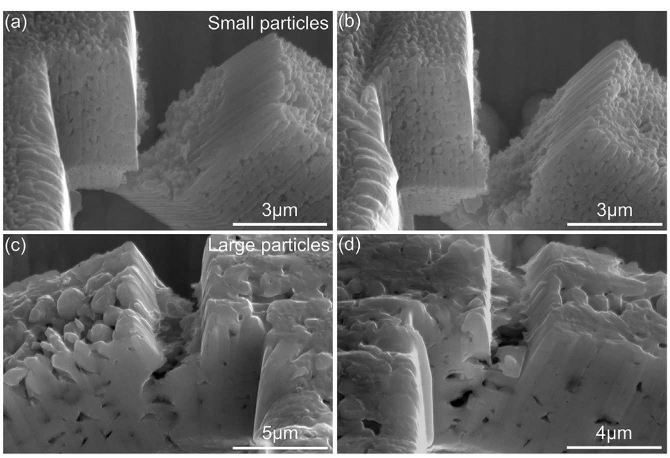

Fig. 6. Fracture morphologies of micro-cantilevers prepared from different initial particle sizes: (a, b) small-particle sample; (c, d) large-particle sample.

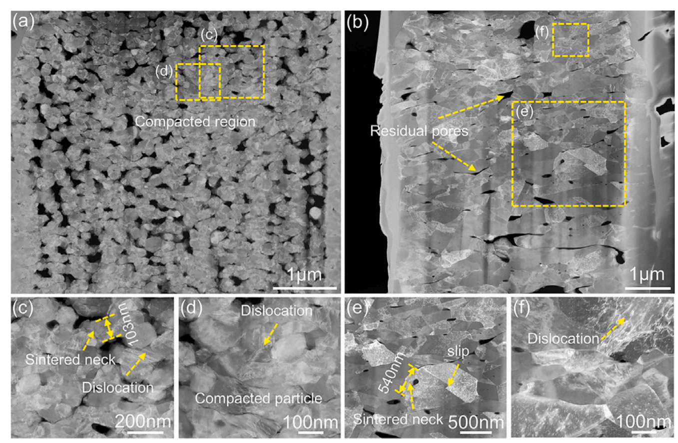

Fig. 7. TEM characterization of sintered Cu structures with different particle sizes: low-magnification images of the (a) small-particle and (b) large-particle samples, and corresponding magnified regions showing sinter necks, residual pores and dislocation structures in (c, d) and (e, f), respectively.

compression direction, indicating that plastic deformation is accommodated not only by pore closure but also by deformation of the Cu particles and sintered necks. In the small-particle sample, the low-magnification image reveals a highly refined particle-neck-pore network with densely distributed residual pores and a compacted central region (Fig. 7a). The magnified images further show fine sintered necks, compressed particles and pronounced dislocation contrast within and near the particle contacts (Fig. 7c and d). The relatively high density of dislocation contrast suggests that plastic deformation is distributed among numerous small particles and necks. Because the characteristic particle size and neck spacing are small, dislocation motion is frequently interrupted by particle boundaries, neck regions and residual pores, promoting the accumulation of dislocations in localized regions.

In contrast, the large-particle sample displays a coarser and more continuous particle-derived framework with fewer but larger residual pores (Fig. 7b). The magnified regions show well-developed sintered necks, evident interparticle sliding traces and dislocation contrast near particle interfaces (Fig. 7e and f). Direct measurements from the scale-calibrated TEM images gave representative post-compression neck widths of approximately 103 nm and 540 nm for the small- and large-particle structures, respectively. Compared with the small-particle structure, the larger particles provide longer internal glide distances before dislocations interact with interfaces or neck boundaries. This favors more pronounced slip within individual particles and along particle-derived interfaces, rather than the formation of a dense and uniformly distributed dislocation network. Such localized slip and interfacial sliding provide a plausible microstructural origin for the lower compressive yield strength of the large-particle sample, because plastic deformation can be activated over larger structural units once the local stress is concentrated at coarse necks or particle interfaces. These TEM observations indicate that particle size strongly modifies the deformation mode of the sintered Cu network: the large-particle structure tends to deform by particle flattening, interfacial sliding and slip over extended particle-scale regions, whereas the small-particle structure promotes more spatially distributed plastic strain. Such particle- and neck-controlled deformation

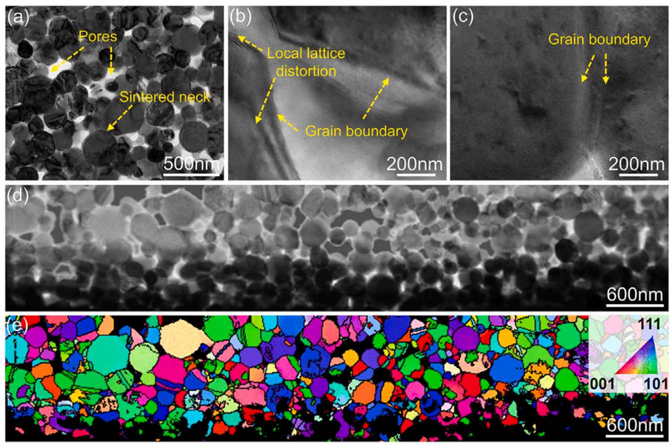

Fig. 8. TEM and PED characterization of the as-sintered small-particle Cu structure: (a) low-magnification TEM image showing residual pores and sintered necks; (b, c) magnified TEM images highlighting grain boundaries and local lattice distortions; (d) cross-sectional TEM image and (e) corresponding PED orientation map.

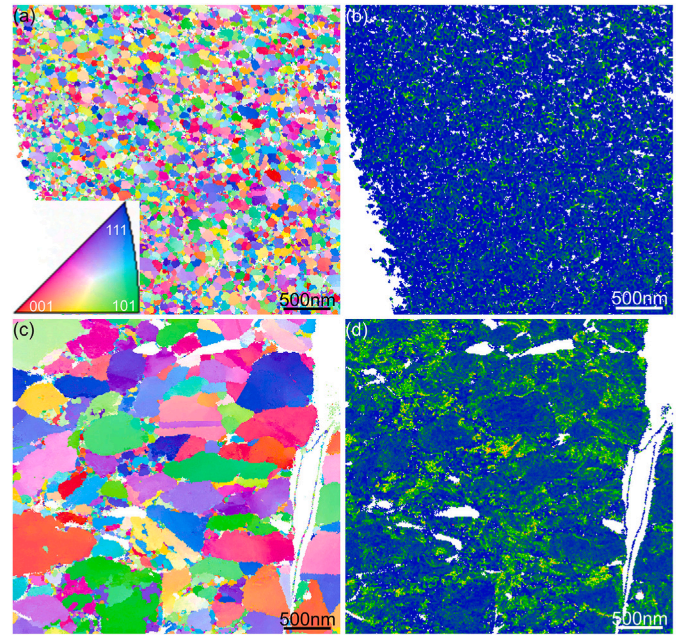

Fig. 9. Post-compression TKD characterization of the sintered Cu structures: (a, b) IPF and corresponding KAM maps of the small-particle structure; (c, d) IPF and corresponding KAM maps of the large-particle structure, revealing crystallographic orientation and local deformation.

is consistent with the general understanding that sintered metallic networks are governed by the connectivity, neck size and residual porosity of the particle skeleton, rather than by the intrinsic response of dense bulk Cu [78].

Fig. 8 characterizes the undeformed small-particle sintered Cu and establishes the crystallographic baseline for interpreting the post-compression TKD results. The bright-field TEM image reveals a porous particle-derived network in which adjacent Cu particles are connected by distinct sintered necks while residual pores remain between incompletely coalesced particles (Fig. 8a). At higher magnification, grain boundaries and associated lattice-distortion contrast are observed within the particles and near bonded regions (Fig. 8b and c). The bright-field image provides a broader view of the connected network (Fig. 8d), while the corresponding orientation map reveals a fine polycrystalline structure with substantial grain-to-grain orientation variation (Fig. 8e). Quantitative analysis of the PED orientation map yielded an area-weighted average grain size of 133 nm, with a maximum measured grain size of 426 nm. The grain-size distribution was concentrated mainly between approximately 50 and 200 nm. The average grain size was smaller than the mean initial powder diameter of 184 nm, confirming that powder particle size and crystallographic grain size represented different structural length scales. The particle-derived units were not necessarily single crystals after sintering, because crystallographic boundaries and orientation discontinuities were retained within and between the bonded particles. The initial powder size primarily defined the geometrical scale of the particle–neck–pore network, whereas the crystallographic grain size affected dislocation motion, storage, and transmission. The sintered necks therefore cannot be regarded simply as geometrical contacts between otherwise undeformed particles; rather, they contain crystallographically heterogeneous regions generated during particle bonding and consolidation. These local orientation discontinuities are expected to influence subsequent slip transmission because dislocations moving between connected particles must interact with both crystallographic grain boundaries and particle-derived interfaces.

The post-compression TKD maps are shown in Fig. 9. The small-particle micropillar retains an exceptionally fine and spatially heterogeneous orientation distribution after deformation (Fig. 9a). Its kernel average misorientation (KAM) map contains densely distributed regions of elevated misorientation throughout the analyzed area (Fig. 9b), indicating widespread deformation-induced lattice curvature. The close spacing of grains and particle-derived interfaces restricts the distance over which crystallographic slip can proceed without interruption. Consequently, strain compatibility between adjacent domains requires frequent changes in slip direction and the storage of geometrically necessary dislocations. The dispersed KAM contrast therefore supports a deformation mode in which plastic strain is partitioned among many fine crystallographic units instead of being accommodated by a limited number of extended slip regions. By comparison, the large-particle micropillar exhibits substantially coarser crystallographic domains (Fig. 9c). Several grains contain continuous intragranular orientation gradients, whereas the corresponding KAM map shows stronger spatial heterogeneity, with elevated values concentrated within selected grains and near particular interfaces (Fig. 9d). The average grain size of the large-particle structure was 539 ± 124 nm, measured along the direction of the uniaxial pressure applied during sintering. The substantially smaller grain size compared with the initial mean particle diameter of 1451 nm is associated with the pronounced deformation and flattening of the particles along this direction during pressure-assisted sintering. The larger characteristic domain size provides a greater distance for dislocation glide and lattice rotation before an interface is encountered. Plastic compatibility is consequently accommodated over larger regions, producing localized orientation gradients rather than the finely dispersed lattice curvature observed in the small-particle sample. This crystallographic localization complements the previously observed particle-scale slip and interfacial deformation without repeating the morphological evidence. It also provides a mechanistic basis for the lower yield resistance of the large-particle structure: once favorably oriented slip systems are activated, deformation can propagate across relatively large domains with fewer interruptions.

3.4. Atomic-scale simulations on deformation mechanisms

Fig. 10 presents the atomistic deformation structures of the compressed sintered Cu micropillar models with different particle sizes. In the small-particle model, the CNA result reveals abundant stacking-fault-related features distributed throughout the micropillar (Fig. 10a). The corresponding dislocation network is dense and spatially dispersed, with dislocations concentrated around particle boundaries and sintered necks (Fig. 10b). These closely spaced interfaces interrupt slip transmission

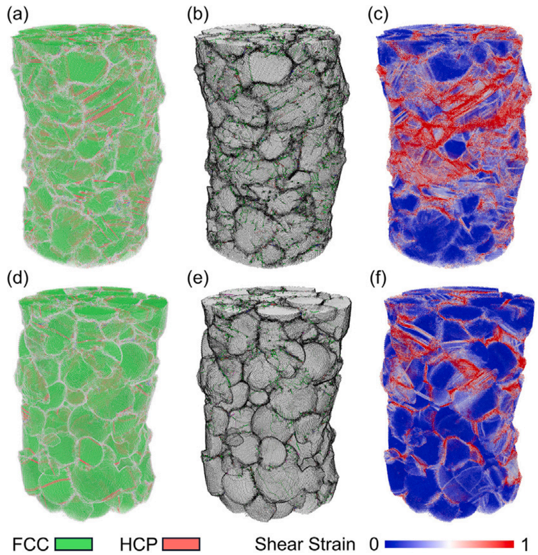

Fig. 10. Atomistic deformation analysis of compressed sintered Cu micropillar models: (a–c) small-particle structure showing (a) CNA configuration, (b) dislocation network, and (c) atomic strain distribution; (d–f) large-particle structure showing (d) CNA configuration, (e) dislocation network, and (f) atomic strain distribution.

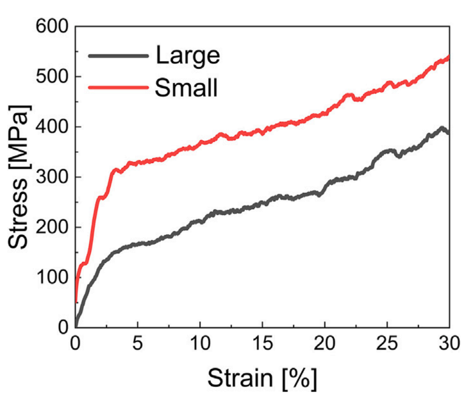

Fig. 11. MD-simulated compressive stress–strain curves of the small- and large-particle sintered Cu micropillar models under uniaxial compression.

and promote repeated nucleation and pinning of partial dislocations within fine particle-neck units. As a result, the atomic strain field is relatively homogeneous, with high-strain regions distributed across the micropillar (Fig. 10c). This deformation mode is consistent with the experimentally observed pore compaction and dislocation accumulation in the small-particle structure. By contrast, the large-particle model shows fewer stacking-fault features and a less uniform dislocation distribution (Fig. 10d and e). The larger particles provide longer glide distances before dislocations and stacking faults are arrested by particle boundaries or neck interfaces. Consequently, plastic deformation is more readily localized along extended slip paths and particle-scale interfaces. This is reflected in the atomic strain map, where high-strain regions concentrate near the side surface and coincide with particle extrusion (Fig. 10f), consistent with the SEM and TEM observations of particle flattening, interfacial sliding and localized deformation in the large-particle sample. These results indicate that particle size controls the balance between dislocation glide and interface-mediated plasticity. Atomistic simulations of nanocrystalline metals have shown that reducing the characteristic structural length scale suppresses long-range intragranular glide and enhances boundary-controlled deformation involving partial dislocations and stacking faults [79].

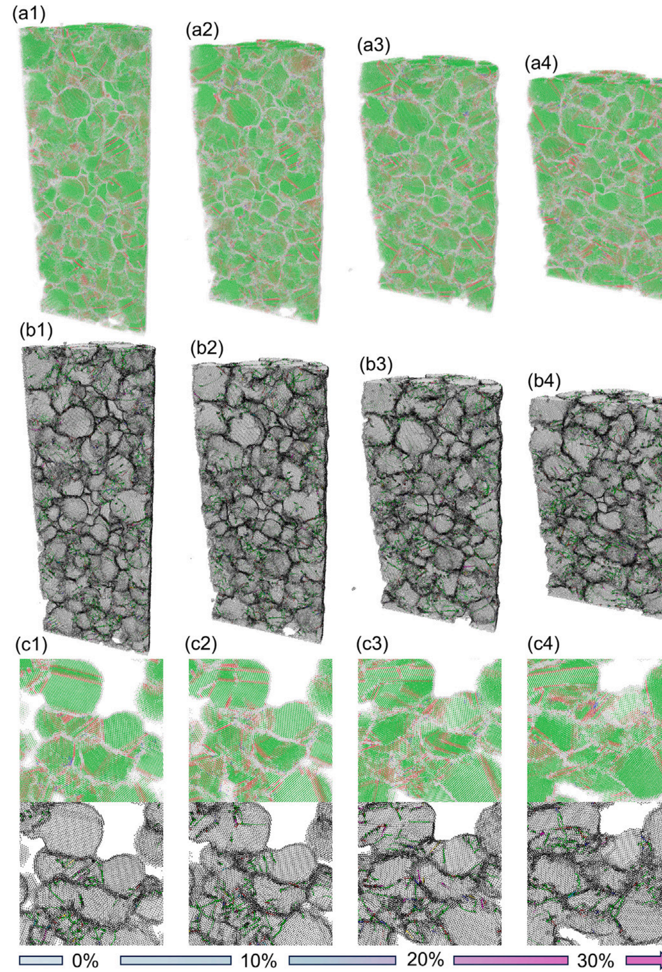

Fig. 12. Compression-induced deformation and defect evolution in the small-particle sintered Cu micropillar model: (a1-a4) CNA configurations; (b1-b4) dislocation structures; (c1-c4) enlarged local deformation views at strains of 0%, 10%, 20% and 30%, respectively.

The simulated stress-strain curves are shown in Fig. 11. After the initial elastic response, the stress of the small-particle micropillar rises rapidly and then increases gradually to above 500 MPa at 30% strain, whereas the large-particle model reaches only about 390 MPa at the same strain. This trend is consistent with the experimental micropillar compression results in Fig. 3, where the small-particle sintered Cu also exhibits a higher yield strength and stronger resistance to post-yield deformation than the large-particle sample. The simulated compression responses qualitatively reproduce the relative mechanical trend obtained from the micropillar tests. The small-particle model maintains a higher flow stress, consistent with the experimentally measured yield strengths of 364 ± 58 MPa and 202 ± 71 MPa for the small- and large-particle structures, respectively. This higher resistance arises from repeated defect interruption and storage at closely spaced particle boundaries and neck regions, whereas the wider interface spacing in the large-particle model permits longer intraparticle defect propagation and promotes strain localization.

The strain-dependent defect evolution in Fig. 12 reveals the origin of this sustained strengthening. In the small-particle model, compression from 0% to 30% strain leads to progressive densification of the particle-neck network, accompanied by continuous generation of stacking faults and dislocations. At low strain, defects first appear around particle contacts and neck regions, where local stress is concentrated during load transfer. With increasing strain, these defects spread into neighboring particles and become increasingly interconnected, forming a distributed

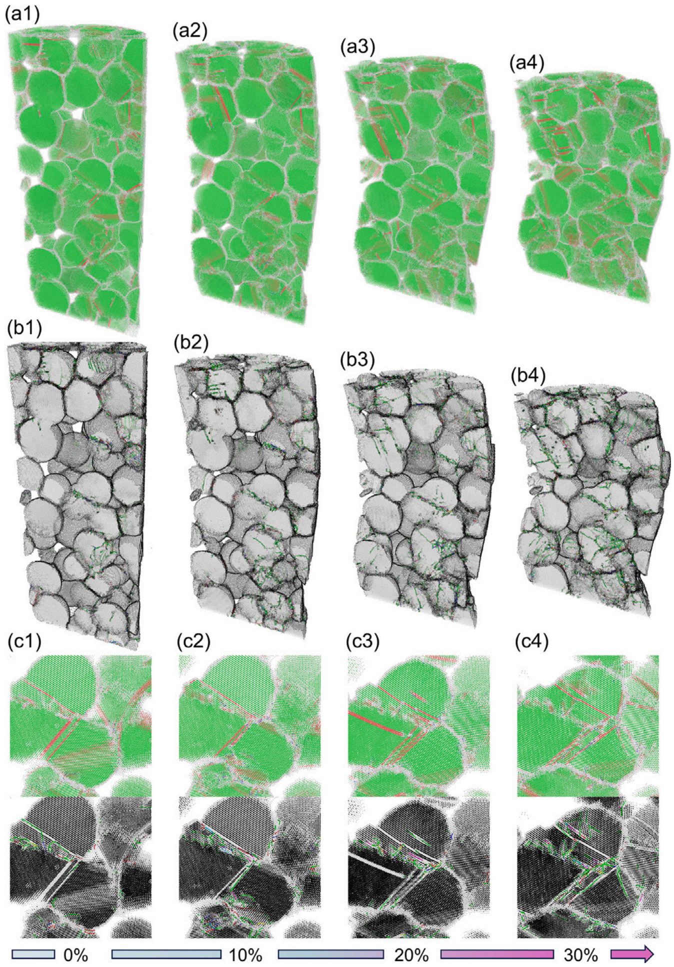

Fig. 13. Compression-induced deformation and defect evolution in the large-particle sintered Cu micropillar model: (a1-a4) CNA configurations; (b1-b4) dislocation structures; (c1-c4) enlarged local deformation views at strains of 0%, 10%, 20% and 30%, respectively.

defect network throughout the micropillar. This behavior is consistent with the concept that reducing the characteristic structural length scale increases the density of interfaces that can nucleate, absorb and block lattice defects, thereby changing plasticity from long-range intragranular glide to interface-mediated deformation [80,81]. The enlarged views further show that individual particles are gradually flattened, while partial dislocations and stacking faults are repeatedly arrested at adjacent particle boundaries and necks. Therefore, plastic deformation proceeds through successive local events across many fine particle-neck units rather than through a single dominant slip path. The strengthening mechanism is also analogous to porous metallic networks, where ligament or neck size and connectivity strongly influence the resistance to plastic flow by controlling defect storage and load transfer [82]. This defect evolution is consistent with the distributed compaction, dense dislocation contrast and dispersed lattice curvature observed experimentally in the small-particle structure. Closely spaced particle boundaries and neck regions repeatedly interrupt the propagation of partial dislocations and their associated stacking faults, thereby distributing defect storage and plastic accommodation across numerous fine particle–neck units.

In contrast, Fig. 13 shows that the large-particle model evolves through a more localized deformation sequence. At the early stage, defects mainly develop within several load-bearing particles and near selected interparticle contacts. As compression proceeds, stacking faults extend over longer distances inside the larger particles, and slip becomes concentrated along specific particle-scale paths. Local particle extrusion and interface sliding become more apparent at higher strain, indicating that strain accommodation is increasingly controlled by a limited number of deforming particles and contacts. Compared with the small-particle network, the lower interface density in the large-particle model reduces the frequency of defect interruption and allows more extended slip before dislocations or stacking faults are blocked by particle boundaries. This progressive localization provides an atomistic explanation for the lower flow stress of the large-particle model in Fig. 11 and supports the experimental observation that large-particle sintered Cu yields more readily under compression. The extended intraparticle defect paths reproduced in the large-particle model are consistent with the localized orientation gradients, particle-scale slip and interfacial displacement observed experimentally. The wider spacing between particle boundaries and neck regions reduces the frequency of defect interruption, allowing plastic strain to concentrate within selected particles and load-bearing contacts. In this context, pinning refers to the repeated arrest of partial dislocations at particle boundaries and neck regions, rather than solute- or precipitate-induced pinning. These closely spaced barriers shorten the effective glide distance and promote defect storage, consistent with grain-boundary-controlled pinning–depinning and grain-size-dependent hardening reported in FCC metals and polycrystalline Cu [83,84]. The experimentally measured structural and mechanical parameters, together with the corresponding deformation features identified by SEM, TEM, TKD, and MD, are summarized in Table S3. Increasing the starting particle size from 184 to 1451 nm was accompanied by an increase in the representative post-compression neck width from approximately 103 to 540 nm and a decrease in the local areal pore fraction from 5.28% to 3.16%. Over the same structural transition, the apparent elastic modulus increased from 12.73 ± 0.48 GPa to 14.54 ± 0.92 GPa, whereas the yield strength decreased from 364 ± 58 MPa to 202 ± 71 MPa. Together with the experimentally observed and atomistically reproduced deformation modes, these opposing mechanical trends demonstrate that stiffness, yielding, deformation localization, and fracture are governed by different aspects of the particle-derived neck–pore architecture rather than by a single monotonic particle-size dependence.

4. Conclusion

The loading-mode-dependent mechanical behavior of pressure-assisted sintered Cu was systematically investigated using micropillar compression tests, micro-cantilever bending tests, SEM, TEM and MD simulations. The main conclusions are as follows:

1. The large-particle sample exhibited a higher apparent elastic modulus (14.5 ± 0.9 GPa), whereas the small-particle sample showed a higher yield strength (364 ± 58 MPa) and greater post-yield deformation resistance. This divergence indicates that elastic stiffness is governed primarily by load-path continuity, while yielding resistance depends more strongly on the characteristic dimensions and spatial distribution of particle-neck units.
2. Micro-cantilever bending tests showed superior fracture resistance in the large-particle structure (5.56 ± 0.14 MPa $\cdot$ m$^{1/2}$) compared to the small-particle structure (1.61 ± 0.16 MPa $\cdot$ m$^{1/2}$). Its greater bending work and post-peak load retention indicate that coarse necks and improved remaining-ligament continuity stabilize crack propagation. In contrast, the fine pore-neck network of the small-particle sample promoted ligament fragmentation and accelerated post-peak degradation.
3. Post-deformation characterization (SEM, TEM, TKD) identified distinct deformation mechanisms in the two structures. The small-particle network accommodated compression through distributed neck deformation, pore compaction and dislocation accumulation, whereas the large-particle structure exhibited localized slip, interfacial sliding and particle extrusion. TKD analyses further

associated the fine structure with dispersed lattice curvature and the coarse structure with localized intragranular orientation gradients.

4. MD simulations reproduced the experimentally observed compression trend and revealed the underlying atomistic deformation mechanisms. The small-particle model sustained a higher flow stress throughout deformation because closely spaced boundaries and necks promoted repeated nucleation, arrest, and accumulation of partial dislocations and stacking faults, leading to distributed plasticity. In contrast, longer slip paths in the large-particle model facilitated intraparticle deformation and strain localization.

In summary, this study offers mechanistic insights into the loading-mode-dependent deformation and fracture of porous sintered Cu. These findings highlight a microstructural design strategy for tailoring particle size, neck connectivity, and pore morphology to balance compressive strength and fracture resistance in sintered Cu interconnects for electronic packaging applications.

CRediT authorship contribution statement

Chenshan Gao: Writing – original draft, Methodology, Investigation. **Leiming Du:** Writing – review & editing, Investigation. **Tianxing Du:** Writing – original draft, Investigation. **Qihang Zong:** Writing – original draft, Investigation. **Shizhen Li:** Investigation. **Huiru Yang:** Investigation. **Guoqi Zhang:** Supervision. **Huaiyu Ye:** Writing – review & editing, Supervision.

Declaration of competing interest

The authors declare that they have no known competing financial interests or personal relationships that could have appeared to influence the work reported in this paper.

Acknowledgements

The authors would like to acknowledge the financial support from 2023TQ07C475, the Shenzhen Major Science and Technology Projects (KJZD20240903102309013), State Key Laboratory of Electrical Insulation, and Power Equipment (EIPE26205), and Shenzhen Polytechnic University Research Fund (Grant No. 6026310016 K). The authors would also like to acknowledge the financial support from the ECSEL Joint Undertaking (JU) under grant agreement No 876659. The JU receives support from the European Union's Horizon 2020 research and innovation program as well as from Germany, Austria, Slovakia, Sweden, Finland, Belgium, Italy, Spain, Netherlands, Slovenia, Greece, France, and Turkey.

Appendix A. Supplementary data

Supplementary data to this article can be found online at doi:10.1016/j.matdes.2026.116856.

Data availability

Data will be made available on request.

References

[1] X. Ji, L. Du, S. He, H. van Zeijl, G. Zhang, Microstructural and micromechanical characterization of sintered nano-copper bump for flip-chip heterogeneous integration, Microelectron. Reliab. 150 (2023) 115180.
[2] S.K. Bhogaraju, F. Conti, H.R. Kotadia, S. Keim, U. Tetzlaff, G. Elger, Novel approach to copper sintering using surface enhanced brass micro flakes for microelectronics packaging, J. Alloys Compd. 844 (2020) 156043.
[3] L. Ma, Z. Lu, Q. Jia, Z. Cui, Y. Wang, D. Li, H. Zhang, G. Zou, F. Guo, Sintering mechanism of bimodal-sized cu nanoparticle paste for power electronics packaging, J. Electron. Mater. 53 (6) (2024) 2988–2998.
[4] S. Krishnan, A. Haseeb, M.R. Johan, Preparation and low-temperature sintering of cu nanoparticles for high-power devices, IEEE Trans. Compon. Packag. Manuf. Technol. 2 (4) (2012) 587–592.
[5] F. Hou, Z. Sun, M. Su, J. Fan, X. You, J. Li, Q. Wang, L. Cao, G. Zhang, Review of die-attach materials for SiC high-temperature packaging, IEEE Trans. Power Electron. 39 (10) (2024) 13471–13486.
[6] H. Cao, J. Yuan, X. Wu, T. Li, L. Wang, J. Suhr, Z. Zhang, Micron-and nano-sized copper sintering pastes: materials, processes, and applications, Mater. Des. 256 (2025) 114291.
[7] T.F. Chen, K.S. Siow, Comparing the mechanical and thermal-electrical properties of sintered copper (cu) and sintered silver (AG) joints, J. Alloys Compd. 866 (2021) 158783.
[8] X. Shi, S. Li, S. Ding, M. Li, J. Sun, K. Li, W. Li, Air-sinterable copper pastes for next-generation electronics: a review, J. Mater. Chem. C 14 (12) (2026) 4696–4710, https://doi.org/10.1039/D5TC04491J
[9] L. Yang, G. Xu, H. Yan, C. Chen, L. Su, K. Li, W. Li, Large-area metal sinter-joining in power electronics packaging: challenges and perspectives, J. Mater. Chem. C 14 (9) (2026) 3414–3426.
[10] W. Liu, X. Wang, J. Zhang, G. Zhang, C. Chen, P. Liu, Quartet structure generation set algorithm based 3D reconstruction on porous structures of sintered copper joints for power electronics packaging, Scr. Mater. 265 (2025) 116750.
[11] W. Chen, X. Liu, D. Hu, X. Zhu, X. Fan, G. Zhang, J. Fan, Unraveling the hydrogen sulfide aging mechanism on electrical-thermal–mechanical property degradation of sintered nanocopper interconnects used in power electronics packaging, Mater. Des. 238 (2024) 112702.
[12] Y. Wang, D. Xu, H. Yan, C.-F. Li, C. Chen, W. Li, Low-temperature copper sinter-joining technology for power electronics packaging: a review, J. Mater. Process. Technol. 332 (2024) 118526.
[13] S.K. Bhogaraju, O. Mokhtari, F. Conti, G. Elger, Die-attach bonding for high temperature applications using thermal decomposition of copper (II) formate with polyethylene glycol, Scr. Mater. 182 (2020) 74–80.
[14] Y.-M. Ju, T.-W. Kim, S.-H. Lee, H.-J. Lee, J. Ahn, H.-S. Kim, Advanced WBG power semiconductor packaging: nanomaterials and nanotechnologies for high-performance die attach paste, Nano Converg. 12 (1) (2025) 38.
[15] J. Xian, Y. Xu, S. Stoyanov, R. Coyle, F.P. Dunne, C. Gourlay, The role of microstructure in the thermal fatigue of solder joints, Nat. Commun. 15 (1) (2024) 4258.
[16] Y. Liu, K. Tu, Low melting point solders based on SN, bi, and in elements, Mater. Today Adv. 8 (2020) 100115.
[17] K.-K. Xu, L. Zhang, L.-L. Gao, N. Jiang, L. Zhang, S.-J. Zhong, Review of microstructure and properties of low temperature lead-free solder in electronic packaging, Sci. Technol. Adv. Mater. 21 (1) (2020) 689–711.
[18] Z. Li, S. Chang, S. Khuje, S. Ren, Recent advancement of emerging nano copper-based printable flexible hybrid electronics, ACS Nano 15 (4) (2021) 6211–6232.
[19] L. Du, G. Schaffar, W. Jiao, K. Liu, R.H. Poelma, V. Maier-Kiener, J. Fan, D. Kiener, W.D. van Driel, X. Fan, et al., Tailoring microstructure and mechanical properties of sintered cu nanoparticles, Acta Mater. (2025) 121501.
[20] X. Liu, S. Li, J. Fan, J. Jiang, Y. Liu, H. Ye, G. Zhang, Microstructural evolution, fracture behavior and bonding mechanisms study of copper sintering on bare DBC substrate for SiC power electronics packaging, J. Mater. Res. Technol. 19 (2022) 1407–1421.
[21] Y. Zuo, A. Robador, M. Wickham, S.H. Mannan, Unraveling the complex oxidation effect in sintered cu nanoparticle interconnects during high temperature aging, Corros. Sci. 209 (2022) 110713.
[22] D. Hu, L. Du, M. Alfreider, J. Fan, D. Kiener, G. Zhang, Microscopic fracture toughness of notched porous sintered cu micro-cantilevers for power electronics packaging, Mater. Sci. Eng. A 897 (2024) 146316.
[23] B. Hou, M. Zhou, X. Zhang, A comprehensive and in-depth study of pressureless and low-temperature in-air sintering performance of bimodal-sized cu nanoparticle pastes for die attachment and the joint strengthening mechanism, J. Mater. Sci. Mater. Electron. 36 (5) (2025) 298.
[24] Y. Zuo, C. Zhao, A. Robador, M. Wickham, S.H. Mannan, Quasi-in-situ observation of the grain growth and grain boundary movement in sintered cu nanoparticle interconnects, Acta Mater. 236 (2022) 118135.
[25] J. Fan, X. Yan, C. Chen, L. Du, Z. Li, J. Zhang, W. Van Driel, G. Zhang, Synchrotron-based nano-CT insights into microscale mechanics of sintered copper nanoparticles, Mater. Res. Lett. (2026) 1–9.
[26] J. Schiøtz, K.W. Jacobsen, A maximum in the strength of nanocrystalline copper, Science 301 (5638) (2003) 1357–1359.
[27] A. Gupta, J. Gruber, S.S. Rajaram, G.B. Thompson, D.L. McDowell, G.J. Tucker, On the mechanistic origins of maximum strength in nanocrystalline metals, NPJ Comput. Mater. 6 (1) (2020) 153.
[28] L. Lu, X. Chen, X. Huang, K. Lu, Revealing the maximum strength in nanotwinned copper, Science 323 (5914) (2009) 607–610.
[29] X. Li, L. Lu, J. Li, X. Zhang, H. Gao, Mechanical properties and deformation mechanisms of gradient nanostructured metals and alloys, Nat. Rev. Mater. 5 (9) (2020) 706–723.
[30] L. Wang, K. Du, C. Yang, J. Teng, L. Fu, Y. Guo, Z. Zhang, X. Han, In situ atomic-scale observation of grain size and twin thickness effect limit in twin-structural nanocrystalline platinum, Nat. Commun. 11 (1) (2020) 1167.
[31] T. Fang, W. Li, N. Tao, K. Lu, Revealing extraordinary intrinsic tensile plasticity in gradient nano-grained copper, Science 331 (6024) (2011) 1587–1590.
[32] Z. Cheng, L. Bu, Y. Zhang, H. Wu, T. Zhu, H. Gao, L. Lu, Unraveling the origin of extra strengthening in gradient nanotwinned metals, Proc. Natl. Acad. Sci. 119 (3) (2022) e2116808119.

[33] Z. Yin, X. Yang, X. Ma, J. Moering, J. Yang, Y. Gong, Y. Zhu, X. Zhu, Strength and ductility of gradient structured copper obtained by surface mechanical attrition treatment, Mater. Des. 105 (2016) 89–95.
[34] Z. Shan, E. Stach, J. Wiezorek, J. Knapp, D. Follstaedt, S. Mao, Grain boundary-mediated plasticity in nanocrystalline nickel, Science 305 (5684) (2004) 654–657.
[35] M.D. Uchic, D.M. Dimiduk, J.N. Florando, W.D. Nix, Sample dimensions influence strength and crystal plasticity, Science 305 (5686) (2004) 986–989.
[36] Z. Shan, R.K. Mishra, S. Syed Asif, O.L. Warren, A.M. Minor, Mechanical annealing and source-limited deformation in submicrometre-diameter ni crystals, Nat. Mater. 7 (2) (2008) 115–119.
[37] H. Tang, K. Schwarz, H. Espinosa, Dislocation-source shutdown and the plastic behavior of single-crystal micropillars, Phys. Rev. Lett. 100 (18) (2008) 185503.
[38] J.R. Greer, W.D. Nix, Nanoscale gold pillars strengthened through dislocation starvation, Phys. Rev. B—Condens. Matter Mater. Phys. 73 (24) (2006) 245410.
[39] M.R. Mazlan, N.H. Jamadon, A. Rajabi, A.B. Sulong, I.F. Mohamed, F. Yusof, N.A. Jamal, Necking mechanism under various sintering process parameters–a review, J. Mater. Res. Technol. 23 (2023) 2189–2201.
[40] R. Gao, H. Tatsumi, T. Kobatake, M. Ueshima, H. Nishikawa, Study on pore features in sintered die-attach microstructures based on machine learning, Sci. Rep. 16 (1) (2026) 8803.
[41] C. Chen, K. Suganuma, Microstructure and mechanical properties of sintered AG particles with flake and spherical shape from nano to micro size, Mater. Des. 162 (2019) 311–321.
[42] D. Hu, Z. Cui, J. Fan, X. Fan, G. Zhang, Thermal kinetic and mechanical behaviors of pressure-assisted cu nanoparticles sintering: a molecular dynamics study, Results Phys. 19 (2020) 103486.
[43] L. Du, W. Jiao, O. Bäcke, M.H. Colliander, R.H. Poelma, J. Fan, W.D. van Driel, X. Fan, G. Zhang, Interface strength and crack propagation mechanisms in sintered copper nanoparticles, Acta Mater. 296 (2025) 121187.
[44] W. Liu, Y. Liu, Y. Cheng, L. Chen, L. Yu, X. Yi, H. Duan, Unified model for size-dependent to size-independent transition in yield strength of crystalline metallic materials, Phys. Rev. Lett. 124 (23) (2020) 235501.
[45] C. Griesbach, S.-J. Jeon, D.F. Rojas, M. Ponga, S. Yazdi, S. Pathak, N. Mara, E.L. Thomas, R. Thevamaran, Origins of size effects in initially dislocation-free single-crystal silver micro-and nanocubes, Acta Mater. 214 (2021) 117020.
[46] X. Liu, H. Nishikawa, Low-pressure cu-cu bonding using in-situ surface-modified microscale cu particles for power device packaging, Scr. Mater. 120 (2016) 80–84.
[47] T. Yonezawa, Q. Zuo, Copper particle sintering for low-temperature electronic joining: a review of materials design and processing strategies, Adv. Eng. Mater. (2026) e202502392.
[48] J. Liu, H. Chen, H. Ji, M. Li, Highly conductive cu–cu joint formation by low-temperature sintering of formic acid-treated cu nanoparticles, ACS Appl. Mater. Interfaces 8 (48) (2016) 33289–33298.
[49] H. Kim, J.-H. Lee, Effects of fine cu particle size on sinter-bondability in die bonding using cu paste possessing effective reducing formulation, Metals 15 (4) (2025) 379.
[50] X. Liu, S. Li, C. Tan, C. Gao, Y. Liu, H. Ye, G. Zhang, Coalescence kinetics and microstructure evolution of cu nanoparticles sintering on substrates: a molecular dynamics study, J. Mater. Res. Technol. 17 (2022) 1132–1145.
[51] J. Xu, S. Das, A.D. Pathak, A. Patra, S. Shetty, D. Hohl, R. Car, Dynamic metal–support interaction dictates cu nanoparticle sintering on al_2O_3 surfaces, ACS Nano 19 (32) (2025) 29242–29254.
[52] X. Chen, C. Li, B. Li, Y. Ying, S. Ye, D.N. Zakharov, S. Hwang, J. Fang, G. Wang, Y.-J. Hu, et al., Surface self-diffusion induced sintering of nanoparticles, ACS Nano 18 (45) (2024) 31160–31173.
[53] P.-H. Chen, H. Wang, K. Li, C.-M. Wang, C.-Y. Liu, A.T. Wu, Sintering of cu nanoparticles for optimized particle size and enhanced interconnect performance, J. Taiwan Inst. Chem. Eng. 173 (2025) 106185.
[54] R. Wu, X. Zhao, Y. Liu, Atomic insights of cu nanoparticles melting and sintering behavior in CuCu direct bonding, Mater. Des. 197 (2021) 109240.
[55] X. Milhet, A. Nait-Ali, D. Tandiang, Y.-J. Liu, D. Van Campen, V. Caccuri, M. Legros, Evolution of the nanoporous microstructure of sintered AG at high temperature using in-situ X-ray nanotomography, Acta Mater. 156 (2018) 310–317.
[56] C. Chen, S. Nagao, K. Suganuma, J. Jiu, T. Sugahara, H. Zhang, T. Iwashige, K. Sugiura, K. Tsuruta, Macroscale and microscale fracture toughness of microporous sintered AG for applications in power electronic devices, Acta Mater. 129 (2017) 41–51.
[57] L. Du, K. Liu, D. Hu, O. Bäcke, X. Hu, X. Ji, J. Fan, R.H. Poelma, M.H. Colliander, G. Zhang, Microstructural and mechanical anisotropy in pressure-assisted sintered copper nanoparticles, Acta Mater. 287 (2025) 120772.
[58] T. Du, C. Gao, O. Bäcke, L. Wei, H. Ye, G. Zhang, M.H. Colliander, L. Du, Particle morphology-dependent deformation mechanisms in sintered cu structures, Mater. Sci. Eng. A (2026) 150688.
[59] I. Annual Reviews, Annual Review of Materials Research, 2009.
[60] S.-H. Li, Y. Zhao, J. Radhakrishnan, U. Ramamurty, A micropillar compression investigation into the plastic flow properties of additively manufactured alloys, Acta Mater. 240 (2022) 118290.
[61] K. Kishida, M. Morisaki, M. Ito, Z. Wang, H. Inui, Room-temperature deformation of single crystals of WC investigated by micropillar compression, Acta Mater. 260 (2023) 119302.
[62] F.R. Wagner, R. Watanabe, R. Schampers, D. Singh, H. Persoon, M. Schaffer, P. Fruhstorfer, J. Plitzko, E. Villa, Preparing samples from whole cells using focused-ion-beam milling for cryo-electron tomography, Nat. Protoc. 15 (6) (2020) 2041–2070.
[63] O. Buchnev, J.A. Grant-Jacob, R.W. Eason, N.I. Zheludev, B. Mills, K.F. MacDonald, Deep-learning-assisted focused ion beam nanofabrication, Nano Lett. 22 (7) (2022) 2734–2739.
[64] C. Berger, M. Dumoux, T. Glen, N.B.-Y. Yee, J.M. Mitchels, Z. Patáková, M.C. Darrow, J.H. Naismith, M. Grange, Plasma FIB milling for the determination of structures in situ, Nat. Commun. 14 (1) (2023) 629.
[65] Y. Zhang, M. Bartosik, S. Brinckmann, S. Lee, C. Kirchlechner, Direct observation of crack arrest after bridge notch failure: a strategy to increase statistics and reduce FIB-artifacts in micro-cantilever testing, Mater. Des. 233 (2023) 112188.
[66] K. Schmuck, M. Antenreiter, M. Alfreider, D. Kiener, Automatic and time-resolved determination of fracture characteristics from in situ experiments, Mater. Des. 243 (2024) 113038.
[67] N.G. Mathews, A. Lambai, G. Mohanty, N. Venkataramani, G. Dehm, B.N. Jaya, Effect of stiff substrates on enhancing the fracture resistance of barium titanate thin films, Mater. Des. 235 (2023) 112440.
[68] R.H. Dodds Jr, T.L. Anderson, M.T. Kirk, A framework to correlate a/W ratio effects on elastic-plastic fracture toughness (J c), Int. J. Fract. 48 (1) (1991) 1–22.
[69] M. Mu, G. Wang, F. Xuan, S. Tu, Unified parameter of in-plane and out-of-plane constraint effects and its correlation with brittle fracture toughness of steel, Int. J. Fract. 190 (1) (2014) 87–98.
[70] M. Wurmshuber, M. Alfreider, S. Wurster, M. Burtscher, R. Pippan, D. Kiener, Small-scale fracture mechanical investigations on grain boundary doped ultrafine-grained tungsten, Acta Mater. 250 (2023) 118878.
[71] N. Beets, J. Stuckner, M. Murayama, D. Farkas, Fracture in nanoporous gold: an integrated computational and experimental study, Acta Mater. 185 (2020) 257–270.
[72] R. Lakes, K. Elms, Indentability of conventional and negative poisson's ratio foams, J. Compos. Mater. 27 (12) (1993) 1193–1202.
[73] M. Samykano, S. Selvamani, K. Kadirgama, W. Ngui, G. Kanagaraj, K. Sudhakar, Mechanical property of FDM printed ABS: influence of printing parameters, Int. J. Adv. Manuf. Technol. 102 (9) (2019) 2779–2796.
[74] A. Sharma, R. Kositski, O. Kovalenko, D. Mordehai, E. Rabkin, Giant shape-and size-dependent compressive strength of molybdenum nano-and microparticles, Acta Mater. 198 (2020) 72–84.
[75] C.-C. Wang, J. Ding, Y.-Q. Cheng, J.-C. Wan, L. Tian, J. Sun, Z.-W. Shan, J. Li, E. Ma, Sample size matters for Al88Fe7Gd5 metallic glass: smaller is stronger, Acta Mater. 60 (13–14) (2012) 5370–5379.
[76] J.R. Greer, J.T.M. De Hosson, Plasticity in small-sized metallic systems: intrinsic versus extrinsic size effect, Prog. Mater. Sci. 56 (6) (2011) 654–724.
[77] P. Liu, X. Wei, S. Song, L. Wang, A. Hirata, T. Fujita, X. Han, Z. Zhang, M. Chen, Time-resolved atomic-scale observations of deformation and fracture of nanoporous gold under tension, Acta Mater. 165 (2019) 99–108.
[78] A. Hodge, J. Biener, J. Hayes, P. Bythrow, C. Volkert, A. Hamza, Scaling equation for yield strength of nanoporous open-cell foams, Acta Mater. 55 (4) (2007) 1343–1349.
[79] V. Yamakov, D. Wolf, S.R. Phillpot, A.K. Mukherjee, H. Gleiter, Dislocation processes in the deformation of nanocrystalline aluminium by molecular-dynamics simulation, Nat. Mater. 1 (1) (2002) 45–49.
[80] J. Schiøtz, F.D. Di Tolla, K.W. Jacobsen, Softening of nanocrystalline metals at very small grain sizes, Nature 391 (6667) (1998) 561–563.
[81] H. Van Swygenhoven, P.M. Derlet, A. Frøseth, Stacking fault energies and slip in nanocrystalline metals, Nat. Mater. 3 (6) (2004) 399–403.
[82] B.-N.D. Ngô, A. Stukowski, N. Mameka, J. Markmann, K. Albe, J. Weissmüller, Anomalous compliance and early yielding of nanoporous gold, Acta Mater. 93 (2015) 144–155.
[83] H. Van Swygenhoven, P. Derlet, A. Frøseth, Nucleation and propagation of dislocations in nanocrystalline fcc metals, Acta Mater. 54 (7) (2006) 1975–1983.
[84] C. Sinclair, W. Poole, Y. Bréchet, A model for the grain size dependent work hardening of copper, Scr. Mater. 55 (8) (2006) 739–742.